Supersonic Nozzle Flow Simulations for Particle Coating Applications: Effects of Shockwaves, Nozzle Geometry, Ambient Pressure, and Substrate Location upon Flow Characteristics

Jung-Jae Park, Min-Wook Lee, Sam S. Yoon, Ho-Young Kim, Scott C. James, Stephen D. Heister, Sanjeev Chandra, Woon-Ha Yoon, Dong-Soo Park, and Jungho Ryu

Characteristics of supersonic flow are examined with specific regard to nano-particle thin-film coating. Effects of shockwaves, nozzle geometry, chamber pressure, and substrate location were studied computationally. Shockwaves are minimized to reduce fluctuations in flow properties at the discontinuities across diamond shock structures. Nozzle geometry was adjusted to ensure optimal expansion (i.e., $P_{exit} = P_{ambient}$), where shock formation was significantly reduced and flow kinetic energy maximized. When the ambient pressure was reduced from 1 to 0.01316 bar, the nozzle's diverging angle must be increased to yield the optimum condition of minimized adversed effects. Beyond some critical distance, substrate location did not seem to be a sensitive parameter on flow characteristics when $P_{amb} = 0.01316$ bar; however, overly close proximity to the nozzle exit caused flow disturbances inside the nozzle, thereby adversely affecting coating gas flow.

1. Introduction

The demand for low-cost, thin-film solar cells is growing substantially. Achieving low cost implies that low-temperature deposition methods are preferred over high-temperature techniques to save energy and prevent thermal damage to both coating materials and substrates. Moreover, non-vacuum coating is desirable because of its obvious convenience. Spray or aerosol deposition (Ref 1-4), which propels coating materials (colloidal drops or particles) onto substrates to form thin films, is an attractive option to meet these requirements. There is a growing demand for these spray deposition techniques because the solar cell industry will trade cell efficiency for mass production through low-cost methods (Ref 3).

Both ''cold spray'' and aerosol deposition techniques use supersonic gas flows to accelerate particles whose kinetic energy is converted into bond energy upon substrate impact. The cold spray method typically uses relatively large particles (i.e., ~10 μm or larger) under relatively high nozzle operating pressures (Ref 5-14). On the other hand, for aerosol deposition, a vacuum chamber facilitates high particle speeds (with particle sizes up to a few micron) even at relatively low operating pressures. Cold spray techniques are generally applied to larger devices for corrosion/thermal protection in aerospace and bio-medical applications (Ref 15). Aerosol deposition is used on smaller devices like micro-actuators and high-speed optical modulators. These two low-cost coating techniques are of significant interest to solar cell engineers seeking to reduce manufacturing costs (Ref 16).

Despite the attraction of low-cost deposition methods, their use in the solar cell industry is in its infancy (Ref 3) and there is significant room for improvement; for example, coating particle speed can be increased through simply optimizing the operating conditions. In general, particle speed is proportional to gas speed, which can be maximized by optimizing the nozzle expansion geometry. This optimization is achieved by adjusting the nozzle geometry such that the exit pressure matches the surrounding ambient pressure ($P_e = P_{amb}$). The aerodynamic of the gas

Jung-Jae Park, Min-Wook Lee, Sam S. Yoon, and **Ho-Young Kim**, Department of Mechanical Engineering, Korea University, Seoul 136-713, Korea; **Scott C. James**, Thermal/Fluid Science and Engineering, Sandia National Laboratories, Livermore, CA 94551; **Stephen D. Heister**, School of Aeronautics and Astronautics, Purdue University, West Lafayette, IN 47907; **Sanjeev Chandra**, Department of Mechanical and Industrial Engineering, University of Toronto, 5 King's College Rd., Toronto, ON Canada; and **Woon-Ha Yoon, Dong-Soo Park,** and **Jungho Ryu**, Functional Ceramics Research Group, Korea Institute of Materials Science, 66 Sangnam-Dong, Changwon, Kyungnam 641-831, Korea. Contact e-mail: skyoon@korea.ac.kr.

flow must be characterized to improve the coating environment and, eventually, increase coating efficiency. Although particle characteristics are not included in this work, this study emphasizes and identifies the parameters that most influence gas flow characteristics.

To support the validity of our results, simulations are compared against the experimental data. Next, supersonic flows emanating from under-, optimally-, and over-expanded nozzles are compared with available existing experimental data for the under- and over-expanded cases. As expected, our computations show that under- and over-expanded nozzles produce strong shockwaves while the optimally-expanded nozzle does not. Flow characteristics around shockwaves, such as gas density, streamwise velocity, pressure, and temperature are reported. Optimal nozzle geometries for both ambient and reduced chamber pressures are suggested. Standoff distance between the nozzle exit and coating substrate is another parameter that could influence coating efficiency; its effects are also examined. Our results are consistent with research on rocket nozzles that have been optimized for supersonic flow (Ref 17, 18).

2. Modeling Descriptions

2.1 Governing Equations

These CFD computations are based on the fully nonlinear, compressible Navier-Stokes (NS) equations (Ref 19) that take account of shockwaves, turbulence, and viscous dissipation. The second-order-accurate computations are performed on a 2D domain, which is consistent with the 2D slot-type nozzle used in experiments (Ref 1), not a circular cone-shaped nozzle. The governing equations are the continuity, momentum, energy, and re-normalized group (RNG) k-ε turbulence equations written in Einsteinian notation:

Continuity equation: $\dfrac{\partial}{\partial x_i}(\rho u_i) = 0.$ \hfill (Eq 1)

Momentum equation: $\dfrac{\partial}{\partial x_i}(\rho u_i u_j) = -\dfrac{\partial P}{\partial x_i} + \dfrac{\partial \tau_{ij}}{\partial x_i}.$ \hfill (Eq 2)

Equation of state: $\rho = \dfrac{P_o + P}{\frac{R_u}{M_w} T}.$ \hfill (Eq 3)

Energy equation: $\dfrac{\partial \rho e u_i}{\partial x_i} = -\dfrac{\partial p u_i}{\partial x_i} + \dfrac{\partial (u_j \tau_{ij} - q_i)}{\partial x_i}.$ \hfill (Eq 4)

where ρ, u, P, T, e, τ, q, R_u, and M_w are the gas density, velocity, pressure, temperature, internal energy, viscous shear stress, heat flux, universal gas constant, and molecular weight, respectively. P is the local, static, or ambient pressure and P_o is the $a = \sqrt{\gamma R_u T / M_w}$ stagnation pressure applied at the nozzle inlet boundary. The Mach number is $M = u/a$, and γ is the specific heat ratio. Further details on the numerical procedures and algorithms are available in the Fluent manual (Ref 19).

2.2 Numerical Details

Figure 1 is a schematic of the supersonic nozzle used in this study. Gas properties at the nozzle exit and the upstream stagnation point are denoted with "e" and "o" subscript, respectively. Also, the subscript "c" and "d" refer to converging and diverging section of the nozzle. The ambient pressure, P_{amb}, is varied between near vacuum ($P_{amb} = 0.01316$ bar, based on the experiment of Ref 16) and 1 bar. The standoff distance between the nozzle exit and the substrate is labeled as "S." A frictionless line of symmetry bisects the spanwise direction and cuts the computational cost in half.

For all computations, 121,600 nodes (i.e., 60×800 for the nozzle and 230×320 for the external domain) are used, with minimum grid spacing $\Delta x = 0.003$ mm, which is sufficient to capture the dominant frequency of convective flow as well as the Kolmogorov length scale. Grid sensitivity studies confirmed that the numerical solution is not contingent upon grid resolution when the total number of nodes exceeds about 100,000. No-slip Dirichlet boundary condition are applied along all walls while the
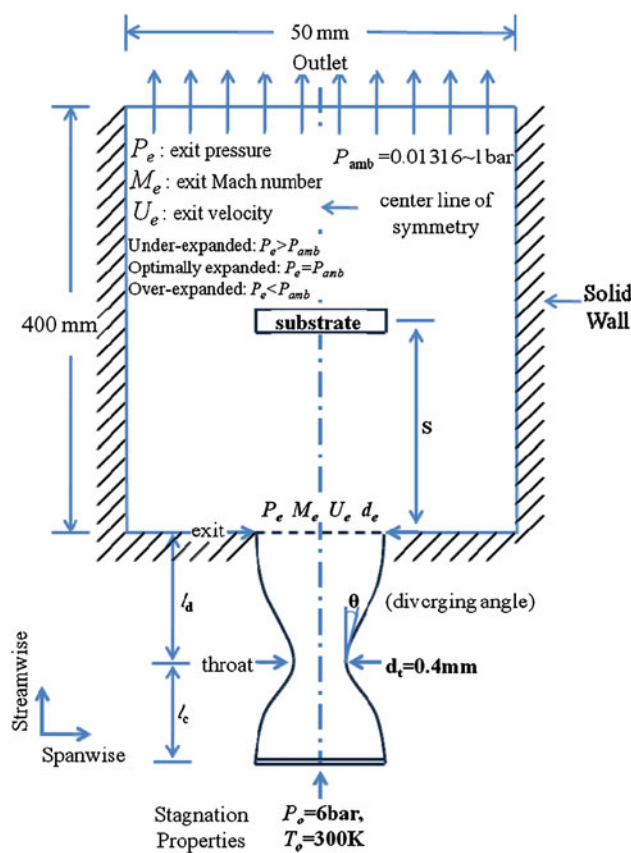

Fig. 1 A schematic of a *de Laval* converging-diverging nozzle. The nozzle stagnation pressure and temperature are set to $P_o = 6$ bar and $T_o = 300$ K. No particles are injected; only the supersonic flow characteristics are examined. A line of symmetry bisects the spanwise direction to cut the computational cost in half. Depending on the nozzle geometry (l_d, l_c, d_e, and d_t) flow characteristics vary from under-, optimal-, and over-expanded nozzles

Neumann boundary condition is used for the outlet. The physical size of the computational domain is 50×400 mm. Stagnation pressure is $P_o = 6$ bar. The working fluid is air at $T_o = 300$ K. The throat diameter is fixed at 0.4 mm, but the exit diameter is either under-, optimally-, or over-expanded with exit diameter 0.56, 0.70, and 1.45 mm, respectively, when $P_{amb} = 1$ bar. The diverging angle, θ, also depends upon the exit diameter. When operating at near vacuum ($P_o = 0.013$ bar), the nozzle exit diameter is 10 mm and yields the optimal pressure of $P_e = P_{amb}$. Note that our results are applicable when the Stokes number (Stk) is small enough that the particle trajectories follow the motion of the gas flow ($Stk < 0.2$). This assumption implies that the particle response time is small and there is little slip between particle and gas (Ref 20). Based on our previous experience with such simulations, the particle speed ranges from 70 to 90% of the gas speed for $Stk < 1$. If $Stk \gg 1$, on the other hand, velocity difference between particles and gas can be significant, for the particles are slow to respond to the gas flow and not easily accelerated.

Coating efficiency may be reduced if particles are *too small*, and end up following the deflected motion of gas near the substrate. There must be a critical Stokes number, Stk_{crit}, that distinguishes whether or not a particle sticks onto the substrate. This is the subject of a future study.

Another parameter that plays an important role in the coating process is the ambient pressure. At low ambient pressure, particle drag is decreased and smaller particles could be used. However, decreasing the ambient pressure alone may not increase particle acceleration unless the nozzle configuration is optimized. Decreasing ambient pressure with fixed nozzle geometry would yield shockwaves and result in reduced gas speeds. Any change in ambient pressure should be accompanied by an updated nozzle geometry optimization.

3. Results and Discussion

3.1 Validation

Figure 2(a) and (b) show the Schlieren and UV-laser-Rayleigh-scattering images, respectively, of supersonic non-isobaric and non-isentropic gas jet from an under-expanded nozzle (Ref 21, 22). The pressure ratio is $P_e/P_{amb} = 2.3$ for the Schlieren image from Zapryagaev et al. (Ref 22) in Fig. 2(a). The UV-laser-Rayleigh-scattering images from Dam et al. (Ref 21) in Fig. 2(b) shows how four periodic diamond structures fit within 26 mm downstream; the white rectangle is the nozzle exit. Our model of the Dam et al. (Ref 21) experiment in Fig. 2(d) correctly approximates the frequency of four diamond shockwaves. The diamond shockwaves dissipate downstream both in the experimental image and in our simulation. Moreover, the model correctly predicts the expansion of the jet downstream.

3.2 Nozzle Geometry Optimization

Our simulations compare the performance of various nozzle geometries maximizing gas speed (i.e., $\sqrt{u^2 + v^2}$ velocity magnitude), which is presumed to be comparable to the impact speed of coating particles ($Stk < 0.2$). Figure 3(a) and (b) show the streamwise and spanwise velocity contours and the under-expanded nozzle's diamond shock structures are evident.

Figure 4 shows the speed contours from the under-, optimally-, and over-expanded nozzles. These simulations demonstrate that the nozzle geometry has a significant effect on flow inside and outside the nozzle. The nozzle pressure ratio (NPR $= P_o/P_e$, where $P_o = 6$ bar) ranges from NPR $= 4.23$ to 5.77 to 7.83 for the under-, optimally-, and over-expanded cases, respectively. In addition, their respective values of exit-to-throat area ratio
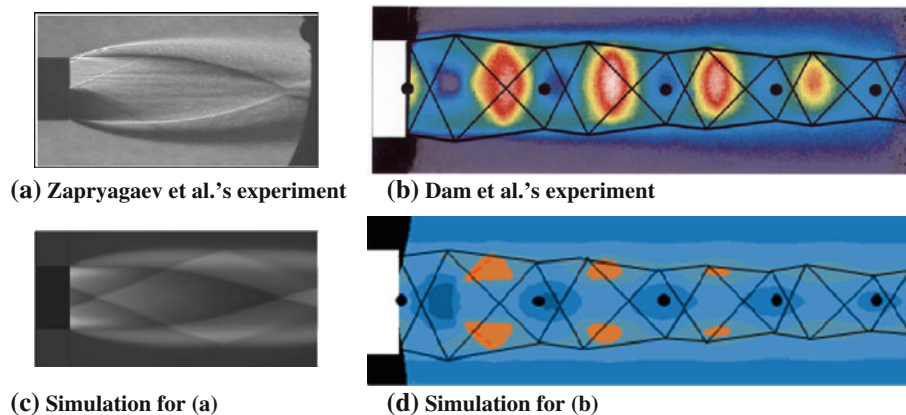

(a) Zapryagaev et al.'s experiment

(b) Dam et al.'s experiment

(c) Simulation for (a)

(d) Simulation for (b)

Fig. 2 Qualitative comparisons between experiments and our simulation results for the supersonic non-isobaric and non-isentropic gas jet for the under-expanded nozzle. (a) Details for the Zapryagaev et al. (Ref 22) nozzle: a conical nozzle with a 15° half-angle at a design Mach number of 3. The nozzle exit inner and outer diameter are 30 and 32 mm, respectively. The nozzle exit pressure is $n = P_e/P_{amb} = 2.3$. (b) Generation of diamond shockwaves exiting from Dam et al.'s (Ref 21) under-expanded nozzle. The snapshot is taken on the time scale of the duration of the laser pulse (18 ns). The nozzle stagnation pressure is 3 bar. Lines indicate shock and expansion waves while dots represent the density maxima
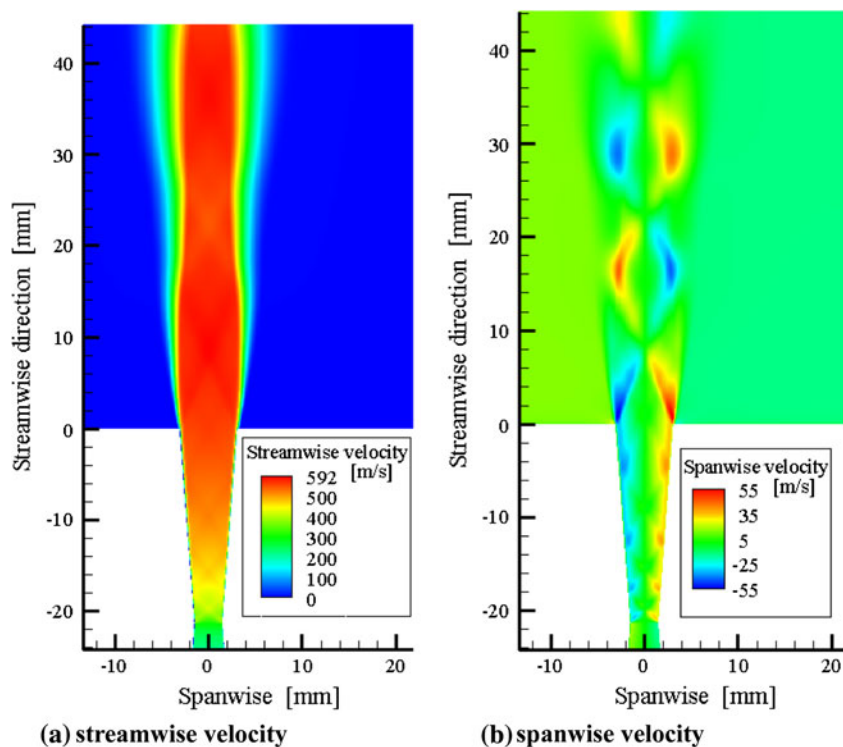
Fig. 3 Propagation of shockwaves generated inside the under-expanded nozzle. Nozzle dimensions are $l_c = 10.0$ mm, $l_d = 21.33$ mm, $d_t = 3.0$ mm, $d_e = 6.2$ mm, and $\theta = 4.290°$. The nozzle exit location is at $x = 0$ mm
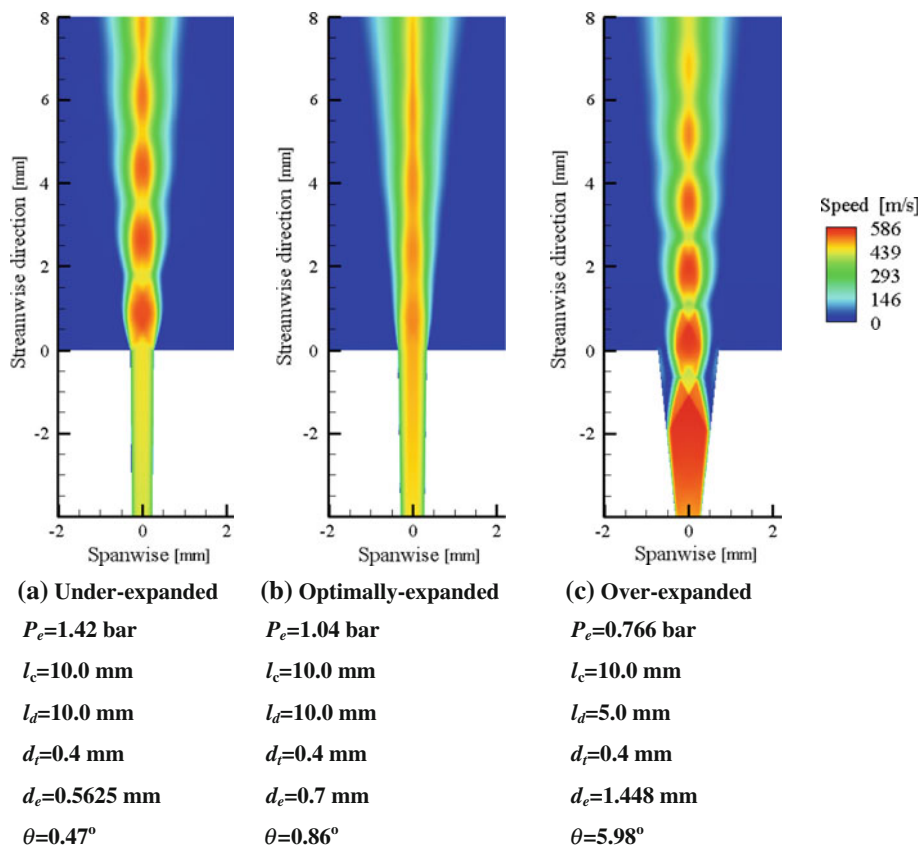

(a) Under-expanded	**(b) Optimally-expanded**	**(c) Over-expanded**
$P_e = 1.42$ bar	$P_e = 1.04$ bar	$P_e = 0.766$ bar
$l_c = 10.0$ mm	$l_c = 10.0$ mm	$l_c = 10.0$ mm
$l_d = 10.0$ mm	$l_d = 10.0$ mm	$l_d = 5.0$ mm
$d_t = 0.4$ mm	$d_t = 0.4$ mm	$d_t = 0.4$ mm
$d_e = 0.5625$ mm	$d_e = 0.7$ mm	$d_e = 1.448$ mm
$\theta = 0.47°$	$\theta = 0.86°$	$\theta = 5.98°$

Fig. 4 Effects of nozzle geometry on supersonic flow characteristics when $P_{amb} = 1$ bar. The nozzle exit is located at $x = 0$ mm

(AR $= A_e/A_t = (d_e/d_t)^2$ with $d_t = 0.4$ mm) are 1.98, 3.06, and 13.10. Note that NPR is presented as a function of exit pressure (P_e) instead of the ambient pressure (P_{amb}) to avoid large values of NPR when the ambient pressure is 0.013 bar. The pattern of alternating low- and high-density regions (diamond shock structures) are observed for the under- and over-expanded nozzles. These structures are most pronounced near the nozzle exit and dissipate downstream. Mach disks near the under- and over-expanded nozzle exits contribute to reduction in flow speeds. In general, the under-expanded nozzle is prone to expansion while exiting the nozzle because of the higher pressure of the ejecting gas; i.e., $P_e > P_{amb}$. When $P_e = P_{amb}$ (optimally-expanded case), shockwaves are suppressed and flow kinetic energy is maximized.

Figure 5 shows the flow properties (density, streamwise velocity, absolute pressure, and temperature) along the nozzle centerlines for the under-, optimally-, and over-expanded nozzles of Fig. 4. All gas properties fluctuate across shockwaves, but fluctuations are minimal for the optimally-expanded case. Although it is minimal, complete removal of these fluctuations could not be achieved at this stage of research. Smooth transitions inside all nozzles are shown for all gas properties until the gas nears the nozzle exit. These fluctuations are amplified as soon as the exiting gas interacts with the gas outside the nozzle. Note that the nozzle exit is located at $x = 0$ mm and the nozzle throat is located at $x = -10$, -10, and -5 mm for

the under-, optimally-, and over-expanded nozzles, respectively. As shown in Fig. 5, it is in the diverging section where decreasing stagnation pressure and temperature are converted into kinetic energy for a supersonic nozzle.

3.3 Effects of Ambient Pressure and Substrate Location

Optimal nozzle geometries were specified through hand calibration for atmospheric and vacuum ambient pressures subject to a nozzle operating absolute pressure of $P_o = 6$ bar. Figure 6 shows the speed contours of flow inside a vacuum chamber, $P_{amb} = 0.01316$ bar, with nozzle geometry optimized to $d_e = 10$ mm. The nozzle length from throat to exit (diverging section) is 30 mm (it was 21.33 mm for the system in atmospheric ambient pressure of Fig. 3). The exit gas properties are $U_e = 648$ m/s, $P_e = 0.0132$ bar, and $M_e = 3.87$, averaged over the exit plane. The maximum gas speed along the centerline is $U_{max} = 724$ m/s. Fluctuations in gas properties (which are induced by pressure gradient between exiting gas and surrounding gas) are minimal. Figure 7 shows the speed distribution across the nozzle exit ($x = 0$ mm) and at downstream locations of $x = 10$ and 20 mm. This nearly square distribution, especially at the nozzle exit, reflects the inviscid nature of the supersonic flow; there is only a thin boundary layer near the nozzle wall due to small
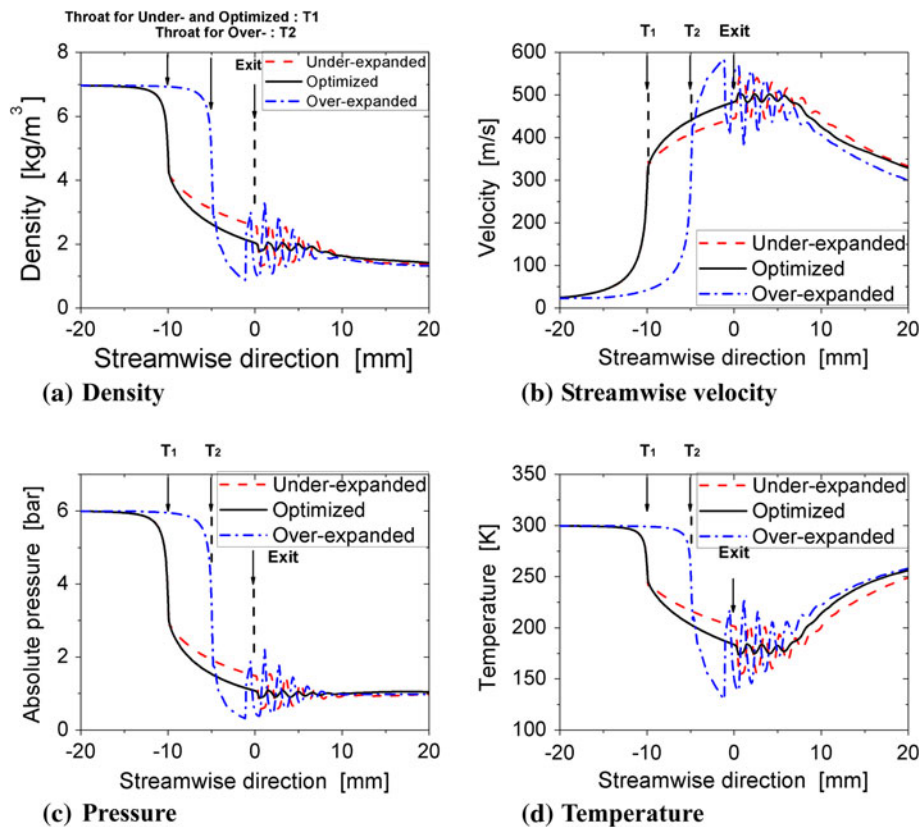

Fig. 5 Supersonic flow characteristics for the under-, optimal, and over-expanded nozzles in conjunction with Fig. 4
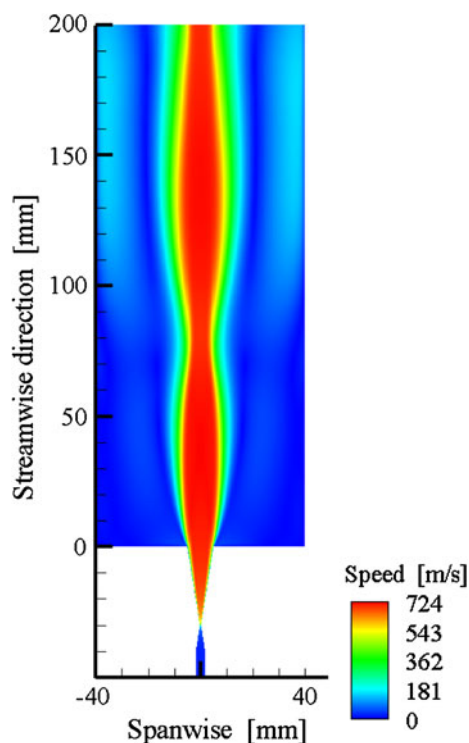
Fig. 6 Speed contour for the optimized nozzle when $P_{amb} = 0.013$ bar. Nozzle dimensions are $l_c = 10.0$ mm, $l_d = 30.0$ mm, $d_t = 0.4$ mm, $d_e = 10.0$ mm, and $\theta = 9.09°$. The exit location is at $x = 0$ mm

effect of viscosity. Figure 8 also shows that even under low ambient pressure ($P_{amb} = 0.0132$), gas is entrained into the jet due to drag and the jet slightly expands downstream in the spanwise direction.

To investigate how substrate location affects flows, a wall is placed $S/d_e = 3$, 9, and 15 downstream, as shown in Fig. 8. Intuitively, one might suppose that the smaller the S, the larger the maximum impact speed because of the substrate's proximity to the nozzle exit. However, a quantitative comparison across Fig. 9 reveals that the gas
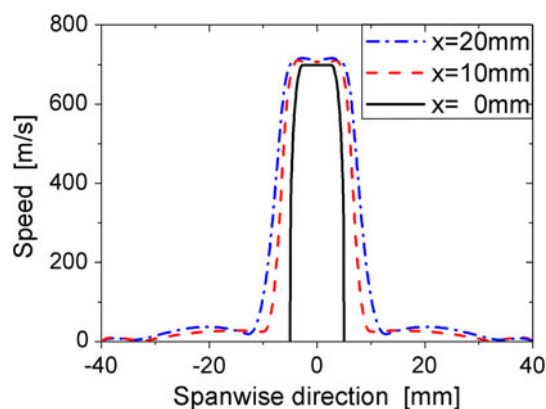
Fig. 7 Speed distribution at the nozzle ($x = 0$ mm) and downstream locations, $x = 10$ and 20 mm. Jet relaxation is shown while entraining flow outside the nozzle
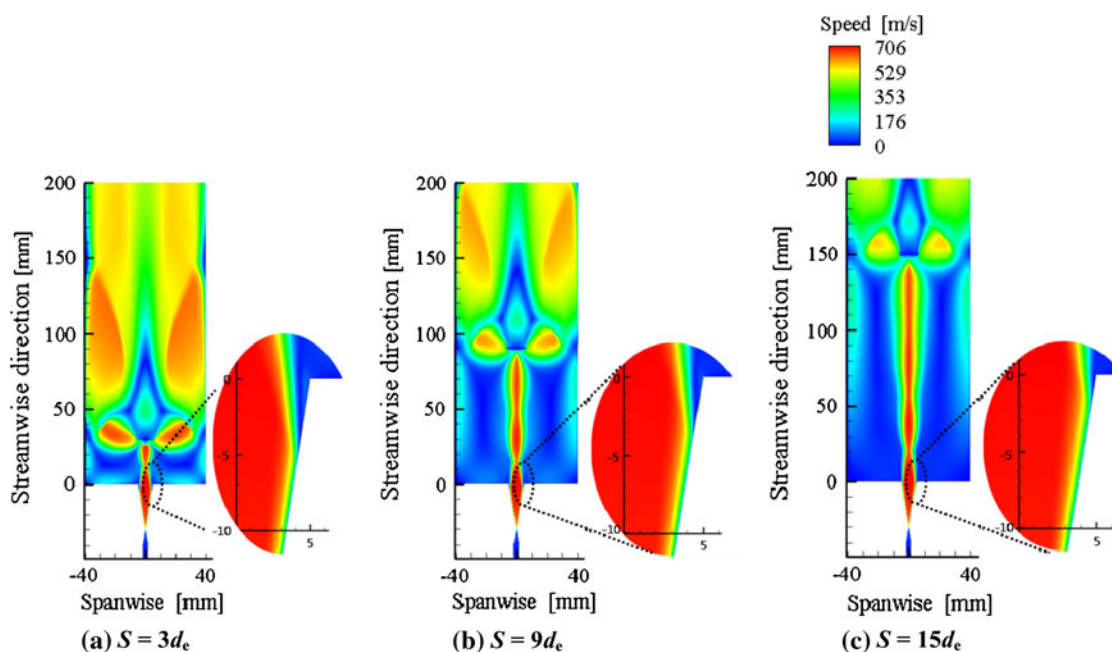

(a) $S = 3d_e$ (b) $S = 9d_e$ (c) $S = 15d_e$

Fig. 8 The effect of substrate location on flows near nozzle exit. Nozzle dimensions are $l_c = 10.0$ mm, $l_d = 30.0$ mm, $d_t = 0.4$ mm, and $d_e = 10.0$ mm. The exit location is at $x = 0$ mm

speed at the substrate does not differ significantly; all distances result in speeds of about 700 m/s. One important observation is that moving the substrate too close to the nozzle exit affects upstream flow, as illustrated in the magnified views of Fig. 8; the high-speed region is slightly narrowed by the infiltration of the low-speed region toward the nozzle edge. Another potential problem is that shockwaves may travel upstream and undermine the performance of the nozzle if the substrate is too close to the nozzle exit.

If ambient pressure (P_{amb}) is ever adjusted, the nozzle exit diameter should be altered appropriately maintain optimized conditions. In Fig. 10, the nozzle optimized for $P_{amb} = 0.01316$, 0.5, and 1.0 bar with substrate located at
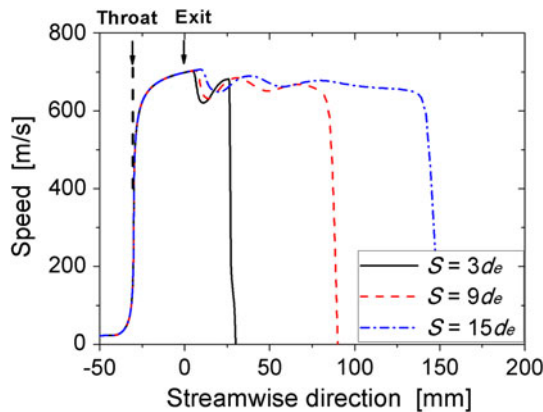

Fig. 9 The variation in maximum speed in the streamwise direction as a function of the substrate location

$S/d_e = 9$. As expected, flow kinetic energy is significantly degraded. Moreover, the nozzle exit diameter is large enough such that ambient gas infiltrates.

Figure 11 quantitatively compares the centerline flow properties for the various ambient pressures used in Fig. 10. As expected, density, streamwise velocity, absolute pressure, and temperature of the accelerating gas decrease because thermal and pressure energy are converted into kinetic energy. Differences in absolute pressure ($P_{abs} = P_{gage} + P_{amb}$, where $P_{gage} = 5$ bar) in Fig. 11(c) are almost solely due to variation in the ambient pressure. The streamwise velocities subject to increased ambient pressure ($P_{amb} = 0.5$ and 1.0 bar) are significantly reduced and severe fluctuations are observed inside the nozzle because of shock formation and flow separation from the nozzle walls.

3.4 Bow Shock Effects

As mentioned previously, shocks adversely affect the performance of the coating process by reducing the kinetic energy of the gas. Across a normal shock, gas density increases [see Eq (4) and (5) from (Ref 6)], which in turn increases drag on particles, thereby slowing them (Ref 23). As the particle's final impact velocity controls the coating efficiency, the appearance of a bow shock right before the substrate is an issue for cold spray coating techniques.

Figure 12 shows a helium jet impacting a substrate located 10 mm downstream of the nozzle exit. The nozzle's operating condition are $P_o = 20$ bar and $T_o = 298$ K yielding a stagnation density of $\rho_{o,He} = 3.23$ kg/m³. The surrounding gas is also helium at $P_{amb} = 1$ bar,
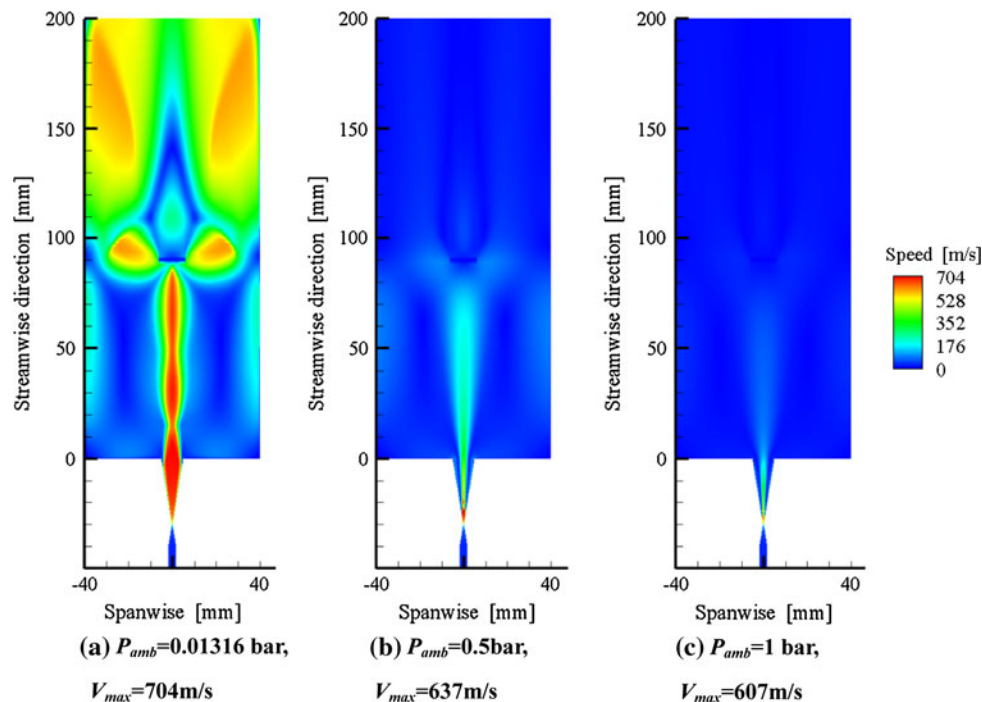

Fig. 10 Effects of ambient pressure on flow characteristics when $P_{amb} = 0.013$, 0.5, and 1.0 bar. Nozzle dimensions are $l_c = 10.0$ mm, $l_d = 30.0$ mm, $d_t = 0.4$ mm, and $d_e = 10.0$ mm. The exit location is at $x = 0$ mm
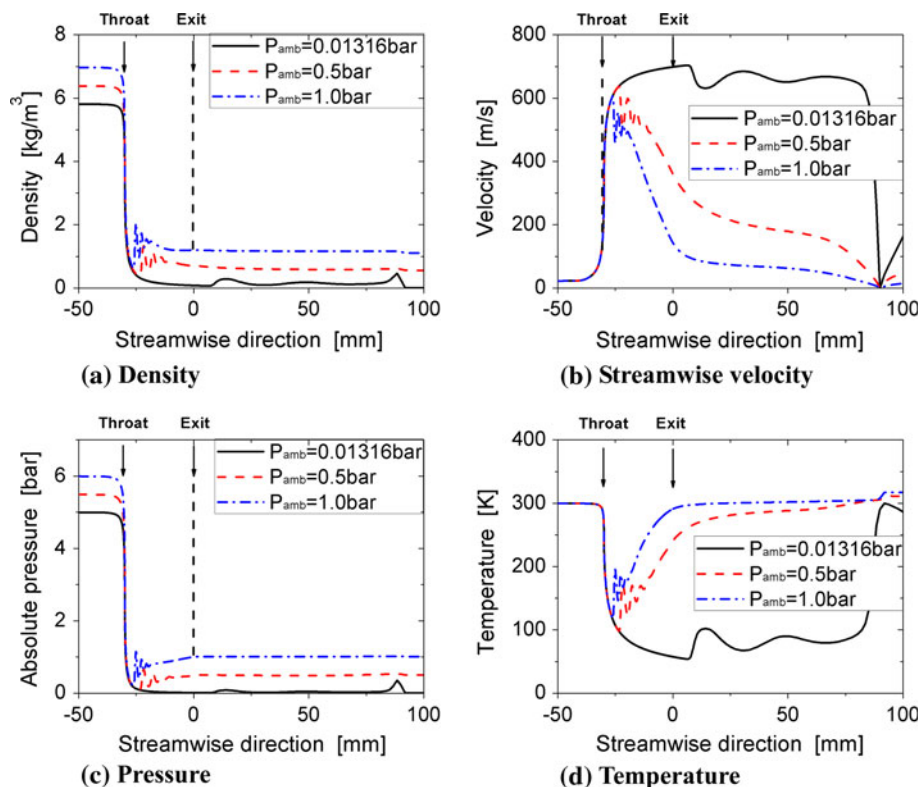
Fig. 11 Supersonic flow characteristics for the under-, optimal, and over-expanded nozzles in conjunction with Fig. 10
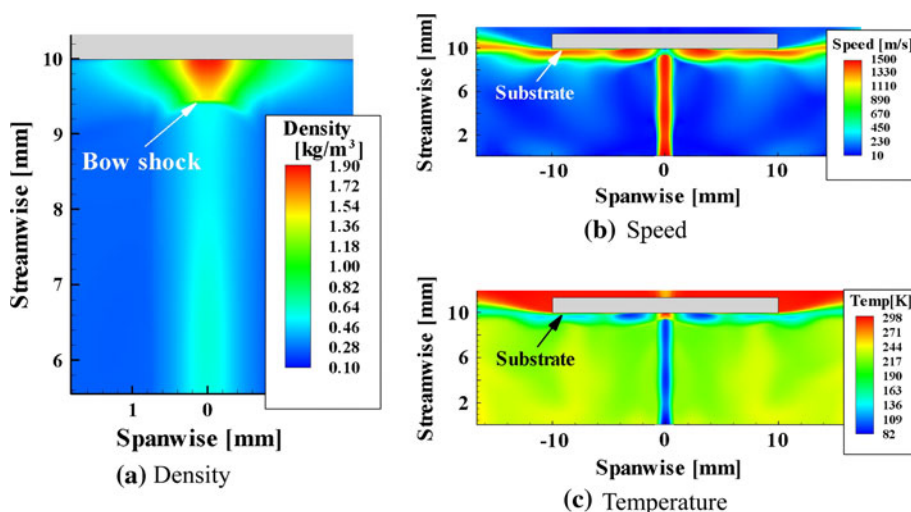

Fig. 12 Bow shock: Density, speed, and temperature distribution of the helium gas injected into a helium chamber ($\rho_{He} = 0.1625$ kg/m^3) when collided with a substrate located 10 mm downstream from the nozzle exit. Nozzle dimensions are $l_c = 10.0$ mm, $l_d = 10.0$ mm, $d_t = 0.2$ mm, $d_e = 1.5$ mm, and $\theta = 3.72°$ under the nozzle's stagnation properties of $P_o = 20$ bar and $T_o = 298$ K. The exit location is at $x = 0$ mm

$T_{amb} = 298$ K, and $\rho_{amb,He} = 0.165$ kg/m^3. The helium jet flows toward the substrate as shown in Fig. 12(a) and bow shock is evident right before the substrate, causing a sudden density increase. However, this density increase (reaching a maximum value of 1.9 kg/m^3) does not recover the original stagnation density of 3.23 kg/m^3 because of losses through non-isentropic shocks (Ref 6) and viscous

shear-layer dissipation between the streaming jet and surrounding gas. In the stagnation region behind the bow shock, particles are slowed due to a sudden increase in drag from the denser gas. Care should be taken not to use particles that are too small to minimize the effects in the bow shock region that could prevent particles from adhering onto the substrate.

Figure 12(b) shows the jet streaming outward radially upon impact. The jet speed is significantly reduced in the bow shock region (<1000 m/s), but quickly recovers its momentum while protruding outwardly. If apply an isentropic flow, the stagnation properties are to be preserved in which case the velocity and temperature should be inversely proportional. Thus, as expected, temperature is lowest when speed is highest; compare Fig. 12(b) and (c). Because of the lost energy through dissipation, the stagnated temperature at substrate center is less than the original stagnation temperature of $T_o = 298$ K.

4. Conclusion

This article characterizes the performance of supersonic nozzle flows. Effects of shockwaves, nozzle geometry, chamber pressure, and substrate location have been studied computationally. Nozzle optimization is required because shockwave-induced fluctuations in flow properties can yield non-uniform coating. Nozzle geometry was adjusted to yield the optimum condition of $P_e = P_{amb}$, which significantly reduces shock formation and maximizes kinetic energy. Reducing chamber pressure from $P_{amb} = 1$ to 0.01316 bar necessitates a nozzle with greater diverging angle to remain optimal. Substrate location is a insensitive parameter when $P_{amb} = 0.01316$ bar; although if it is too close to the nozzle exit, flow infiltration and separation inside the nozzle are observed. The adverse effect of the bow shock incurred at the substrate was simulated and discussed.

Acknowledgments

References

1. J. Akedo, Room Temperature Impact Consolidation (RTIC) of Fine Ceramic Powder by Aerosol Deposition Method and Applications to Microdevices, *J. Therm. Spray Technol.*, 2008, **17**, p 181-198

2. S.-Q. Fan, G.-J. Li, C.-X. Li, G.-J. Liu, G.-J. Yang, and L.-Z. Zhang, Preliminary Study of Performance of Dye-Sensitized Solar Cell of Nano-TiO₂ Coating Deposited by Vacuum Cold Spraying, *Mater. Trans.*, 2006, **47**, p 1703-1709

3. S.-Q. Fan, G.-J. Li, G.-J. Yang, L.-Z. Zhang, J.-C. Gao, and Y.-X. Xi, Fabrication of Nano-TiO₂ Coating for Dye-Sensitized Solar Cell by Vacuum Cold Spraying at Room Temperature, *J. Therm. Spray Technol.*, 2007, **16**, p 893-897

4. S.-Q. Fan, G.-J. Yang, C.-J. Li, C.-J. Liu, and L.-Z. Zhang, Characterization of Microstructure of Nano-TiO₂ Coating Deposited by Vacuum Cold Spraying, *J. Therm. Spray Technol.*, 2006, **15**, p 513-517

5. A. Blais, B. Jodoin, J.L. Dorier, M. Gindrat, and C. Hollenstein, Inclusion of Aerodynamic Non-Equilibrium Effects in Supersonic Plasma Jet Enthalpy Probe Measurements, *J. Therm. Spray Technol.*, 2005, **14**, p 342-353

6. B. Jodoin, Cold Spray Nozzle Mach Number Limitation, *J. Therm. Spray Technol.*, 2001, **11**, p 496-507

7. W.Y. Li and C.J. Li, Optimal Design of a Novel Cold Spray Gun Nozzle at a Limited Space, *J. Therm. Spray Technol.*, 2005, **14**, p 391-396

8. M. Karimi, A. Fartaj, G. Randin, D. Vanderzwet, W. Birtch, and J. Villafuerte, Numerical Simulation of the Cold Gas Dynamic Spray Process, *J. Therm. Spray Technol.*, 2006, **15**, p 518-523

9. F. Raletz, M. Vardelle, and G. Ezo'o, Critical Particle Velocity Under Cold Spray Conditions, *Surf. Coat. Technol.*, 2006, **201**, p 1942-1947

10. W.Y. Li, C.-J. Liu, C.X. Wang, and H.S. Bang, Measurement and Numerical Simulation of Particle Velocity in Cold Spraying, *J. Therm. Spray Technol.*, 2006, **15**, p 559-562

11. F. Gartner, T. Stoltenhoff, T. Schmidt, and H. Kreye, The Cold Spray Process and its Potential for Industrial Applications, *J. Therm. Spray Technol.*, 2006, **15**, p 223-232

12. H. Katanoda, M. Fukuhara, and N. Ino, Numerical Study of Combination Parameters for Particle Impact Velocity and Temperature in Cold Spray, *J. Therm. Spray Technol.*, 2007, **16**, p 627-633

13. W.-Y. Li, H. Liao, G. Douchy, and C. Coddet, Optimal Design of a Cold Spray Nozzle by Numerical Analysis of Particle Velocity and Experimental Validation with 316L Stainless Steel Powder, *Mater. Des.*, 2007, **28**, p 2129-2137

14. S.H. Zahiri, W. Yang, and M. Jahedi, Characterization of Cold Spray Titanium Supersonic Jet, *J. Therm. Spray Technol.*, 2009, **18**, p 110-117

15. A. Papyrin, V. Kosarev, K.V. Klinkov, A. Alkhimov, and V.M. Fomin, *Cold Spray Technology*, Elsevier, Oxford, 2006

16. J.-H. Ryu, D.-S. Park, B.-D. Hahn, J.-J. Choi, W.-H. Yoon, K.-Y. Kim, and H.-S. Yun, Photocatalytic TiO₂ Thin Films by Aerosol-Deposition: From Micron-Sized Particles to Nano-Grained Thin Film at Room Temperature, *Appl. Catal. B Environ.*, 2008, **83**, p 1-7

17. J. Mattingly, *Elements of Gas Turbine Propulsion*, McGraw-Hill, Portland, OR, 1996

18. G.P. Sutton and O. Biblarz, *Rocket Propulsion Elements: An Introduction to the Engineering of Rockets*, Wiley, New York, NY, 2001

19. Fluent, User's Guide, 2008

20. C. Crowe, M. Sommerfeld, and T. Yutaka, *Multiphase Flows with Droplets and Particles*, CRC Press, Boca Raton, FL, 1998

21. N.J. Dam, M. Rodenburg, R.A.L. Tolboom, G.G.M. Stoffels, P.M. Huisman-Kleinherenbrink, and J.J. ter Meulen, Imaging of an Underexpanded Nozzle Flow by UV Laser Rayleigh Scattering, *Exp. Fluids*, 1998, **24**, p 93-101

22. V.I. Zapryagaev, A.N. Kudryavtsev, A.V. Lokotok, A.V. Solotchin, A.A. Pavlov, A. Hadjadj, An Experimental and Numerical Study of a Supersonic-Jet-Shock-Wave Structure, *Proceedings of the XI International Conference on the Methods of Aerophysical Research*, Novosibirsk, Russia, 2002, p 187-191

23. J. Pattison, S. Celotto, A. Khan, and W. O'Neil, Standoff Distance and Bow Shock Phenomena in the Cold Spray Process, *Surf. Coat. Technol.*, 2008, **202**, p 1443-1454